Density Functional Theory of Adsorption in Spherical Cavities and Pore Size Characterization of Templated Nanoporous Silicas with Cubic and Three-Dimensional Hexagonal Structures

Peter I. Ravikovitch and Alexander V. Neimark*

Center for Modeling and Characterization of Nanoporous Materials, TRI/Princeton, 601 Prospect Avenue, Princeton, New Jersey 08542-0625

Received May 23, 2001. In Final Form: November 21, 2001

Adsorption in spherical cavities is studied by the nonlocal density functional theory (NLDFT). Theoretical results are compared with experimental data on ordered nanoporous materials with cubic $Pm3n$ (SBA-1, HMM-3), cubic $Im3m$ (SBA-16), and 3D hexagonal $P6_3/mmc$ (SBA-2, SBA-12) cagelike structures. Quantitative comparison shows that capillary condensation of N_2 at 77 K in sufficiently small cavities (pore diameters $3 < D < 6$ nm) occurs reversibly; the equilibrium condensation pressure is determined by the cavity diameter. In the case of hysteretic isotherms on materials with cavity diameters of >ca. 6 nm, the capillary condensation step corresponds to the theoretical limit of stability of the metastable adsorption film. For pores wider than ca. 10 nm, this limit is approximated by the macroscopic Derjaguin−Broekhoff−de Boer equations. Desorption from cavities of >6 nm is controlled by the size of the windows that connect the cavity with the bulk fluid. If the diameter of the window is below ca. 4 nm, desorption occurs via spontaneous cavitation of condensed liquid. We developed a NLDFT method for calculating pore size distributions (PSD) of cavities, the amount of intrawall porosity, and, in combination with X-ray diffraction, the wall thickness in siliceous materials with cagelike pores. We demonstrate that the adsorption method allows one to differentiate between the materials of different morphological symmetry. For regular cagelike structures, the NLDFT results are in remarkably good agreement with the estimates derived from geometrical considerations. In contrast, the conventional Barrett−Joyner−Halenda method of PSD analysis, based on the Kelvin equation, underestimates the pore sizes in cagelike nanopores by up to 100%.

1. Introduction

In recent years, tremendous progress has been made in the synthesis of templated nanoporous materials (TNM) by using ionic and nonionic (block copolymer) surfactants as structure-directing agents to produce periodically ordered inorganic structures.[1−12] The pore structure of TNM retains the symmetry of organic mesophases including hexagonal, bicontinuous cubic, or micellar cubic morphologies encountered in surfactants,[13−20] amphiphilic block copolymers,[21−23] and other supramolecular systems, for example dendrimers.[24,25]

Reliable control of pore structure parameters, such as micro- and mesoporosity, specific surface area, and pore size distribution (PSD) at the nanoscale, is critical for various potential applications of TNM. Gas adsorption is especially suitable for characterization of internal porosity and PSD.[26] In our previous publications,[27−32] we have

* Corresponding author. E-mail: aneimark@triprinceton.org.

(1) Kresge, C. T.; Leonowicz, M. E.; Roth, W. J.; Vartuli, J. C.; Beck, J. S. *Nature* **1992**, *359*, 710.
(2) Beck, J. S.; Vartuli, J. C.; Roth, W. J.; Leonowicz, M. E.; Kresge, C. T.; Schmitt, K. D.; Chu, C. T. W.; Olson, D. H.; Sheppard, E. W.; McCullen, S. B.; Higgins, J. B.; Schlenker, J. L. *J. Am. Chem. Soc.* **1992**, *114*, 10834.
(3) Inagaki, S.; Fukushima, Y.; Kuroda, K. *J. Chem. Soc., Chem. Commun.* **1993**, 680.
(4) Monnier, A.; Schuth, F.; Huo, Q.; Kumar, D.; Margolese, D.; Maxwell, R. S.; Stucky, G. D.; Krishnamurty, M.; Petroff, P.; Firouzi, A.; Janicke, M.; Chmelka, B. F. *Science* **1993**, *261*, 1299.
(5) Hue, Q. S.; Margolese, D. I.; Ciesla, U.; Feng, P. Y.; Gier, T. E.; Sieger, P.; Leon, R.; Petroff, P. M.; Schuth, F.; Stucky, G. D. *Nature* **1994**, *368*, 317.
(6) Tanev, P. T.; Pinnavaia, T. J. *Science* **1995**, *267*, 865.
(7) Attard, G. S.; Glyde, J. C.; Goltner, C. G. *Nature* **1995**, *378*, 366.
(8) Zhao, D. Y.; Feng, J. L.; Huo, Q. S.; Melosh, N.; Fredrickson, G. H.; Chmelka, B. F.; Stucky, G. D. *Science* **1998**, *279*, 548.
(9) Zhao, D. Y.; Huo, Q. S.; Feng, J. L.; Chmelka, B. F.; Stucky, G. D. *J. Am. Chem. Soc.* **1998**, *120*, 6024.
(10) Inagaki, S.; Guan, S.; Fukushima, Y.; Ohsuna, T.; Terasaki, O. *J. Am. Chem. Soc.* **1999**, *121*, 9611.
(11) Kim, J. M.; Stucky, G. D. *Chem. Commun.* **2000**, 1159.
(12) Guan, S.; Inagaki, S.; Ohsuna, T.; Terasaki, O. *J. Am. Chem. Soc.* **2000**, *122*, 5660.
(13) Israelachvili, J. N.; Mitchell, D. J.; Ninham, B. W. *J. Chem. Soc., Faraday Trans. Ii* **1976**, *72*, 1525.
(14) Mariani, P.; Luzzati, V.; Delacroix, H. *J. Mol. Biol.* **1988**, *204*, 165.
(15) Seddon, J. M.; Templer, R. H. *Philos. Trans. R. Soc. London, Ser. A* **1993**, *344*, 377.
(16) Delacroix, H.; Gulik-Krzywicki, T.; Seddon, J. M. *J. Mol. Biol.* **1996**, *258*, 88.
(17) Clerc, M. *J. Phys. II* **1996**, *6*, 961.
(18) Sakya, P.; Seddon, J. M.; Templer, R. H.; Mirkin, R. J.; Tiddy, G. J. T. *Langmuir* **1997**, *13*, 3706.
(19) de Geyer, A.; Guillermo, A.; Rodriguez, V.; Molle, B. *J. Phys. Chem. B* **2000**, *104*, 6610.
(20) Seddon, J. M.; Robins, J.; Gulik-Krzywicki, T.; Delacroix, H. *Phys. Chem. Chem. Phys.* **2000**, *2*, 4485.
(21) Hajduk, D. A.; Harper, P. E.; Gruner, S. M.; Honeker, C. C.; Kim, G.; Thomas, E. L.; Fetters, L. J. *Macromolecules* **1994**, *27*, 4063.
(22) Alexandridis, P.; Olsson, U.; Lindman, B. *J. Phys. Chem.* **1996**, *100*, 280.
(23) Alexandridis, P.; Olsson, U.; Lindman, B. *Langmuir* **1998**, *14*, 2627.
(24) Balagurusamy, V. S. K.; Ungar, G.; Percec, V.; Johansson, G. *J. Am. Chem. Soc.* **1997**, *119*, 1539.
(25) Yeardley, D. J. P.; Ungar, G.; Percec, V.; Holerca, M. N.; Johansson, G. *J. Am. Chem. Soc.* **2000**, *122*, 1684.
(26) Gregg, S. J.; Sing, K. S. W. *Adsorption, Surface Area and Porosity*; Academic Press: New York, 1982.
(27) Ravikovitch, P. I.; Wei, D.; Chueh, W. T.; Haller, G. L.; Neimark, A. V. *J. Phys. Chem. B* **1997**, *101*, 3671.
(28) Neimark, A. V.; Ravikovitch, P. I.; Grun, M.; Schuth, F.; Unger, K. K. *J. Colloid Interface Sci.* **1998**, *207*, 159.
(29) Ravikovitch, P. I.; Haller, G. L.; Neimark, A. V. *Adv. Colloid Interface Sci.* **1998**, *77*, 203.
(30) Ravikovitch, P. I.; Neimark, A. V. *Langmuir* **2000**, *16*, 2419.
(31) Neimark, A. V.; Ravikovitch, P. I. *Microporous Mesoporous Mater.* **2001**, *44−45*, 697.

10.1021/la0107594 CCC: $22.00
Published on Web 01/23/2002

developed the nonlocal density functional theory (NLDFT) of adsorption and capillary condensation in cylindrical nanopores and applied it to the characterization of silica TNM with (a) 2D hexagonal symmetry (*p*6*m* space group) such as MCM-41,[1,2] FSM-16,[3] and SBA-15[8,9] materials and (b) bicontinuous cubic structure centered on the minimal gyroid surface (*Ia*3*d* space group)[4,30,33−35] such as MCM-48[2] materials. Recently, the NLFDT method was extended to micro-mesoporous materials such as SBA-15.[36]

In this paper, we focus on cagelike structures with cubic (*Pm*3*n* and *Im*3*m* space groups) and 3D hexagonal ($P6_3/mmc$ space group) symmetries synthesized as particles and films.[5,9,10,37,38] Examples of cubic materials with *Pm*3*n* symmetry include silica materials of SBA-1[5,39,40] type and HMM-3 hybrid organic−inorganic materials.[12,41] *Im*3*m* symmetry is exemplified by SBA-16 materials.[9,11,42] 3D hexagonal structures with $P6_3/mmc$ symmetry include SBA-2,[43] HMM-2 organosilica,[10] and SBA-12[9] materials and films.[37,38] In addition to these regular materials, there exist less-ordered cagelike structures such as polydisperse micelle templated porous silicas[44] and mesocellular foams[45−48] prepared by microemulsion templating. All these systems contain a network of nanosized cavities connected by narrower channels or windows.

The type of symmetry (*Pm*3*n*, *Im*3*m*, or $P6_3/mmc$) and the lattice constant determined by X-ray diffraction (XRD) do not specify completely the pore structure morphology, which implies certain relationships between the porosity, surface area, and mean pore diameter. Below, we show that the conventional methods of pore size analysis which assume cylindrical shape of pore channels, such as the Barrett−Joyner−Halenda (BJH)[49] method, are not applicable for cagelike structures and that the model of regularly spaced spherical cavities seems to be a reasonable approximation. We develop the NLFDT model for adsorption and capillary condensation in spherical cavities and apply this model for characterization of cagelike structures from low-temperature nitrogen adsorption isotherms.

The paper is organized as follows. In section 2, we review existing macroscopic methods of analysis and interpretation of adsorption isotherms. We critically discuss the Derjaguin−Broekhoff−de Boer (DBdB) theory of capillary condensation in ink-bottle spherical cavities[50] which is the most suitable macroscopic model for the systems under consideration. We show that the DBdB theory does not account for two important sorption mechanisms: (a) equilibrium capillary condensation in sufficiently narrow cavities characterized by a reversible adsorption isotherm and (b) spontaneous desorption/cavitation of condensate characterized by a hysteretic adsorption isotherm with a sharp step on the desorption branch, whose position does not depend on the size of the pore neck/window.

In section 3, we present the NLDFT model for capillary condensation in spherical cavities and demonstrate that the results are in agreement with reversible and hysteretic isotherms of nitrogen on cagelike materials. The NLDFT model predicts the limiting pressures of spontaneous capillary condensation (vaporlike spinodal) and desorption (liquidlike spinodal) and the pressure of equilibrium transition. The NLDFT relations asymptotically merge with the DBdB relations for cavities wider than ca. 10 nm. Comparing the theoretical predictions and the experimental data, we come to the following conclusions. In the case of reversible adsorption (materials with cavity diameters less than ca. 6 nm), the position of the capillary condensation step corresponds to the pressure of equilibrium transition. In the case of hysteretic adsorption (materials with cavity diameters greater than ca. 6 nm), the adsorption branch corresponds to the theoretical isotherm of metastable states which terminates by the spontaneous condensation near the vaporlike spinodal. The desorption step corresponds to the spontaneous evaporation which occurs either at the pressure of equilibrium evaporation from the necks/windows (neck diameters greater than ca. 4 nm) or at the pressure limited by the equilibrium transition pressure and the liquidlike spinodal pressure (neck diameters less than ca. 4 nm).

In section 4, we present the NLDFT method for pore size distribution calculations in spherical cavities and apply it for pore size analysis in cagelike structures of SBA-1, HMM-3, SBA-2, SBA-12, and SBA-16 materials. In section 5, we review the geometrical models of cagelike structures with cubic and 3D hexagonal symmetries. We show good agreement between the NLDFT calculations and the estimates based on the geometrical methods. Several prominent examples are presented to demonstrate that the NLDFT method can be used not only for the pore size and surface area calculations but also for the discrimination between possible pore structure morphologies. The results are summarized in section 6.

2. Background: Macroscopic Models for Adsorption Characterization of Materials with Spherical Cavities

Pore geometry significantly affects thermodynamic properties of confined fluids and their adsorption behavior.[51,52] As compared to cylindrical pores, spherical pores of the same diameter exert a stronger confinement that causes a shift of the capillary condensation transition to lower relative pressures.[50] Broekhoff and de Boer[50] used the augmented Kelvin−Cohan equation to study conden-

(32) Ravikovitch, P. I.; Neimark, A. V. *Colloids Surf., A* **2001**, *187−188*, 11.
(33) Alfredsson, V.; Anderson, M. W.; Ohsuna, T.; Terasaki, O.; Jacob, M.; Bojrup, M. *Chem. Mater.* **1997**, *9*, 2066.
(34) Carlsson, A.; Kaneda, M.; Sakamoto, Y.; Terasaki, O.; Ryoo, R.; Joo, S. H. *J. Electron Microsc.* **1999**, *48*, 795.
(35) Schumacher, K.; Ravikovitch, P. I.; Du Chesne, A.; Neimark, A. V.; Unger, K. K. *Langmuir* **2000**, *16*, 4648.
(36) Ravikovitch, P. I.; Neimark, A. V. *J. Phys. Chem. B* **2001**, *105*, 6817.
(37) Lu, Y. F.; Ganguli, R.; Drewien, C. A.; Anderson, M. T.; Brinker, C. J.; Gong, W. L.; Guo, Y. X.; Soyez, H.; Dunn, B.; Huang, M. H.; Zink, J. I. *Nature* **1997**, *389*, 364.
(38) Doshi, D. A.; Huesing, N. K.; Lu, M. C.; Fan, H. Y.; Lu, Y. F.; Simmons-Potter, K.; Potter, B. G.; Hurd, A. J.; Brinker, C. J. *Science* **2000**, *290*, 107.
(39) Kim, M. J.; Ryoo, R. *Chem. Mater.* **1999**, *11*, 487.
(40) Goletto, V.; Imperor, M.; Babonneau, F. *Stud. Surf. Sci. Catal.* **2000**, *129*, 287.
(41) Sayari, A.; Hamoudi, S.; Yang, Y.; Moudrakovski, I. L.; Ripmeester, J. R. *Chem. Mater.* **2000**, *12*, 3857.
(42) Zhao, D. Y.; Yang, P. D.; Melosh, N. A.; Feng, J. L.; Chmelka, B. F.; Stucky, G. D. *Adv. Mater.* **1998**, *10*, 1380.
(43) Hue, Q.; Leon, R.; Petroff, P. M.; Stucky, G. D. *Science* **1995**, *268*, 1324.
(44) Kramer, E.; Forster, S.; Goltner, C.; Antonietti, M. *Langmuir* **1998**, *14*, 2027.
(45) Lukens, W. W.; Schmidt-Winkel, P.; Zhao, D. Y.; Feng, J. L.; Stucky, G. D. *Langmuir* **1999**, *15*, 5403.
(46) Schmidt-Winkel, P.; Lukens, W. W.; Yang, P. D.; Margolese, D. I.; Lettow, J. S.; Ying, J. Y.; Stucky, G. D. *Chem. Mater.* **2000**, *12*, 686.
(47) Schmidt-Winkel, P.; Glinka, C. J.; Stucky, G. D. *Langmuir* **2000**, *16*, 356.
(48) Lettow, J. S.; Han, Y. J.; Schmidt-Winkel, P.; Yang, P. D.; Zhao, D. Y.; Stucky, G. D.; Ying, J. Y. *Langmuir* **2000**, *16*, 8291.
(49) Barrett, E. P.; Joyner, L. G.; Halenda, P. P. *J. Am. Chem. Soc.* **1951**, *73*, 373.
(50) Broekhoff, J. C. P.; de Boer, J. H. *J. Catal.* **1968**, *10*, 153.
(51) Evans, R.; Marconi, U. M. B.; Tarazona, P. *J. Chem. Soc., Faraday Trans. Ii* **1986**, *82*, 1763.
(52) Balbuena, P. B.; Gubbins, K. E. *Charact. Porous Solids III* **1994**, *87*, 41.

sation and desorption in ink-bottle pores, considered as spherical cavities connected by narrow cylindrical necks/windows. This approach is equivalent to the Derjaguin[53] approximation. According to the DBdB theory, the equilibrium thickness of the adsorbed film h in a spherical pore of radius R_P is determined from the balance of capillary and disjoining pressures:[50]

$$\Pi(h)\, V_L + \frac{2\gamma V_L}{R_P - h} = RT \ln(P_0/P) \qquad (1)$$

Here, P/P_0 is the relative pressure in the bulk gas; γ and V_L are the surface tension and the molar volume of liquid, and $\Pi(h)$ is the disjoining pressure of the adsorbed film. Note that omitting the disjoining pressure term we obtain the Kelvin−Cohan equation for a spherical interface. The disjoining pressure isotherm, which effectively accounts for the solid−fluid interactions, is given in the form of the Frenkel−Halsey−Hill equation,[26]

$$\ln(P_0/P) = \frac{V_L\, \Pi(h)}{RT} = \frac{K}{h^m} \qquad (2)$$

with the parameters $K = 44.54$ and $m = 2.241$ (h is in Å)[54] to approximate nitrogen adsorption on nonporous silica and other oxides at 77 K (see ref 31 for details).

According to eqs 1 and 2, capillary condensation in a spherical cavity, which is connected to the neighboring pores through narrow windows (ink-bottle pore model), is always associated with a hysteresis. Indeed, it is assumed that during adsorption, the isotherm traces a sequence of metastable states of the adsorption film, and the capillary condensation occurs spontaneously when the film thickness approaches the limit of stability. The critical thickness of metastable films is determined from the condition[50]

$$-\left(\frac{d\Pi(h)}{dh}\right)_{h=h_{cr}} = \frac{2\gamma}{(R_P - h_{cr})^2} \qquad (3)$$

Desorption from a cavity is delayed until the vapor pressure is reduced below the equilibrium desorption pressure from the pore window, which leads to a pronounced hysteresis effect. Thus, while the capillary condensation condition is determined by the size of the cavity, the desorption condition is related to the size of the window. A simplified version of the Broekhoff−de Boer model for ink-bottle pores has been used for pore size characterization of mesocellular foams[45,48] to determine the PSD of cavities from the adsorption branch of the isotherm and the PSD of windows from the desorption branch.

However, the DBdB scenario of capillary condensation in spherical cavities deserves revisiting. First, if the size of the window is small enough, the decrease in the vapor pressure may cause the fluid in the cavity to become thermodynamically unstable at a higher pressure than the equilibrium desorption pressure for the pore window. In this case, the confined fluid may cavitate and evaporate spontaneously. This effect would cause a sharp knee on the desorption isotherm. It is well documented in the adsorption literature that the lower closure point of the hysteresis loop is practically independent of the adsorbent structure and determined primarily by the fluid and temperature.[26] This observation gave rise to a hypothesis that fluid trapped in a cavity blocked by smaller pores attains its spinodal point (tensile strength hypothesis).[55] For nitrogen adsorption, the lower closure point of the hysteresis loop is usually identified in the range of relative pressure between $P/P_0 = 0.42$ and 0.48. A typical example of this phenomenon is presented below, in Figure 4, in which we plotted the experimental isotherm on a sample of SBA-16 material.[42] In this example, desorption practically does not occur until the pressure is reduced below ca. $P/P_0 = 0.48$. In this situation, the desorption pressure is not likely to be related to the size of blocking pores, and therefore the desorption branch is not suitable for the PSD analysis.

Another important addition to the classical picture of adsorption in spherical pores comes from the recent experimental data that suggest that the capillary condensation in spherical cavities does not necessarily imply a hysteretic isotherm. For example, the nitrogen adsorption isotherm on HMM-3 material with sufficiently small cagelike pores[12] exhibits a completely reversible adsorption−desorption step (see Figure 5 below), which we incline to interpret as a capillary condensation transition. The reversibility of the step indicates an equilibrium transition. In the DBdB theory, the equilibrium condition between the adsorbed film and liquid in a spherical pore is given by[50]

$$RT \ln(P_0/P) = \frac{3\gamma V_L + \dfrac{3V_L}{(R_P - h_e)^2}\displaystyle\int_{h_e}^{R_P} (R_P - h)^2\, \Pi(h)\, dh}{R_P - h_e} \qquad (4)$$

Equation 4 has to be solved together with eq 1 to determine the equilibrium relative pressure and corresponding film thickness. However, in the Broekhoff−de Boer description there is no provision for the equilibrium transition actually taking place in experiments because the authors assumed that "there is no means of establishing an equilibrium path of desorption in the case of spheroidal cavities".[50]

3. NLDFT of Capillary Condensation and Hysteresis in Spherical Cavities

Molecular level models, such as the density functional theory, give a more complete picture of phase transitions in pores than the classical thermodynamic methods (see e.g. ref 56 for review). To model capillary condensation and desorption of nitrogen in spherical cavities, we adopted the NLDFT of Tarazona.[57,58] For slit and cylindrical geometries, this model has been shown to provide reliable results, in quantitative agreement with molecular simulations[59,60] and experimental data on regular MCM-41 and SBA-15 materials.[31,32,61] Henderson and Sokolowski[62] performed density functional theory calculations and demonstrated the main qualitative features of adsorption in model spherical pores. However, their study did not address the problem of hysteresis and no comparison was

(53) Derjaguin, B. V. *Acta Phys.-Chim.* **1940**, *12*, 181.
(54) Dubinin, M. M.; Kataeva, L. I.; Ulin, V. I. *Bull. Acad. Sci. USSR, Div. Chem. Sci.* **1977**, *26*, 459.
(55) Burgess, C. G. V.; Everett, D. H. *J. Colloid Interface Sci.* **1970**, *33*, 611.
(56) Evans, R. *J. Phys.: Condens. Matter* **1990**, *2*, 8989.
(57) Tarazona, P. *Phys. Rev. A* **1985**, *31*, 2672.
(58) Tarazona, P.; Marconi, U. M. B.; Evans, R. *Mol. Phys.* **1987**, *60*, 573.
(59) Neimark, A. V.; Ravikovitch, P. I.; Vishnyakov, A. *Phys. Rev. E* **2000**, *62*, R1493.
(60) Ravikovitch, P. I.; Vishnyakov, A.; Neimark, A. V. *Phys. Rev. E* **2001**, *64*, 011602.
(61) Ravikovitch, P. I.; O'Domhnaill, S. C.; Neimark, A. V.; Schuth, F.; Unger, K. K. *Langmuir* **1995**, *11*, 4765.
(62) Henderson, D.; Sokolowski, S. *Phys. Rev. E* **1995**, *52*, 758.

Table 1. Parameters of the NLDFT Model for N_2 Adsorption on Silica at 77 K (References 28 and 29)

fluid−fluid interactions[a]			solid−fluid interactions[b]	
ϵ_{ff}/k_B (K)	σ_{ff} (Å)	d_{HS} (Å)	$\rho_S\epsilon_{sf}/k_B$ (K/Å^2)	σ_{sf} (Å)
94.45	3.575	3.575	22.53	3.17

[a] ϵ_{ff}/k_B and σ_{ff} are the well depth and the distance parameter of the Lennard-Jones potential, respectively. Fluid−fluid interactions are truncated at $5\sigma_{ff}$. d_{HS} is the diameter of hard spheres. [b] $\rho_S\epsilon_{sf}/k_B$ and σ_{sf} are the energetic and distance parameters of the N_2−silica interactions, respectively.

made with macroscopic thermodynamic theories or experimental data.

3.1. Theory and Parameters. In the NLDFT approach, the adsorption and desorption isotherms in pores are calculated based on the intermolecular potentials of fluid−fluid and solid−fluid interactions. The local density of the adsorbate, confined in a pore at given chemical potential μ and temperature T, is determined by the minimization of the grand thermodynamic potential Ω:

$$\Omega[\rho(\mathbf{r})] = F_{HS}[\rho(\mathbf{r})] + \frac{1}{2}\int\int d\mathbf{r}\, d\mathbf{r}'\, \rho(\mathbf{r})\, \rho(\mathbf{r}') \times \Phi_{attr}(|\mathbf{r} - \mathbf{r}'|) - \int d\mathbf{r}\, \rho(\mathbf{r})[\mu - U_{ext}(\mathbf{r})] \quad (5)$$

The first term on the right-hand side of eq 5, $F_{HS}[\rho(\mathbf{r})]$, is the nonlocal free energy functional for hard spheres;[57,58] the second term is the mean-field free energy due to the Lennard-Jones (LJ) attractive interactions; $\Phi_{attr}(\mathbf{r})$ is calculated according to the Weeks−Chandler−Andersen scheme;[63] $U_{ext}(\mathbf{r})$ is the potential imposed by the pore walls.

The solid−fluid potential $U_{ext}(\mathbf{r})$ for silica walls is the result of LJ interactions with the outer layer of oxygen atoms in the wall of a spherical cavity of radius R (measured to the centers of the first layer of atoms in the pore wall). The potential at a distance x from the wall is obtained by integrating the LJ 12-6 potential over the spherical surface:[62,64,65]

$$U_{ext}(x,R) = 2\pi\rho_s\epsilon_{sf}\sigma_{sf}^2\left[\frac{2}{5}\sum_{i=0}^{9}\left(\frac{\sigma_{sf}^{10}}{R^i x^{10-i}} + (-1)^i\frac{\sigma_{sf}^{10}}{R^i(x-2R)^{10-i}}\right) - \sum_{i=0}^{3}\left(\frac{\sigma_{sf}^{4}}{R^i x^{4-i}} + (-1)^i\frac{\sigma_{sf}^{4}}{R^i(x-2R)^{4-i}}\right)\right] \quad (6)$$

Here, ϵ_{sf} and σ_{sf} are the energetic and scale parameters of the potential, respectively; ρ_s is a number of oxygen atoms per unit area of the pore wall. For $R \to \infty$, eq 6 reduces to the 10-4 potential for a plane surface. The intermolecular potential parameters for nitrogen were established in our previous works on the NLDFT modeling of adsorption in siliceous materials with cylindrical pores.[29,59] With these parameters, the calculated adsorption isotherm on a flat substrate follows the standard nitrogen adsorption isotherm on nonporous oxides given by eq 2[54,66] (see plot in ref 29). The parameters of the fluid−fluid interactions are taken from our previous works[28,61] (Table 1). These parameters describe the bulk equilibrium of nitrogen, surface tension included.

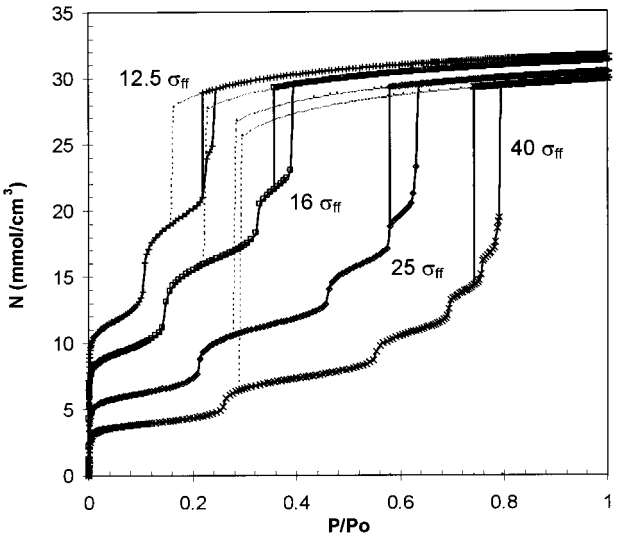

Figure 1. Selected NLDFT nitrogen isotherms at 77.4 K in silica spherical pores of different diameters. The theoretical hysteresis loops are bounded by the lines of spontaneous condensation (right), equilibrium (middle), and spontaneous desorption (left) transitions.

We consider spherically symmetric density distributions. For a density distribution $\rho(r)$, where $r = R - x$ is a radial coordinate from the pore center, excess adsorption per unit of "internal" pore volume is calculated as

$$N_V^{ex} = \frac{3}{(R - \sigma_{OO}/2)^3}\int_0^R \rho(r)\, r^2\, dr - \rho_{bulk} \quad (7)$$

Here, $\sigma_{OO}/2 = 0.138$ nm is the effective radius of an oxygen atom in the silica wall; ρ_{bulk} is the bulk gas density at a given relative pressure, P/P_0. The pore diameters reported below are internal, $D_{in} = 2R - \sigma_{OO}$, when expressed in dimensional units and crystallographic when expressed in units of the molecular diameter of nitrogen, $2R/\sigma_{ff}$.

3.2. NLDFT Adsorption−Desorption Isotherms of N_2 at 77 K in Silica Spherical Pores. Figure 1 shows selected NLDFT isotherms in pores of different diameters. On the adsorption branch, as the relative pressure increases, the isotherms exhibit a sequence of steps corresponding to the multilayer formation and a sharp step indicating the capillary condensation. On the desorption branch, as the relative pressure decreases, the desorption step is located at a relative pressure much lower than the capillary condensation step (shown by dotted lines in Figure 1). The capillary condensation and desorption steps on the theoretical isotherms correspond to spontaneous transitions near the vaporlike and liquidlike spinodals, respectively. The equilibrium transition corresponds to the relative pressure at which the vaporlike state on the adsorption branch and the liquidlike state on the desorption branch have equal grand thermodynamic potentials. The pressures of the equilibrium transition are depicted in Figure 1 by vertical lines; they are located between the pressures of the spontaneous condensation and the pressure of the spontaneous desorption. Thus, the states on the adsorption branch above the equilibrium pressure are metastable and so are the states on the desorption branch below the equilibrium pressure.

This behavior of the adsorption isotherms in spherical pores is qualitatively similar to the NLDFT predictions for cylindrical pores.[60,61] There are, however, important quantitative differences due to stronger wall−fluid interactions in spherical pores: (1) the equilibrium and

(63) Weeks, J. D.; Chandler, D.; Andersen, H. C. *J. Chem. Phys.* **1971**, *54*, 5237.
(64) Baksh, M. S. A.; Yang, R. T. *AIChE J.* **1991**, *37*, 923.
(65) Kaminsky, R. D.; Maglara, E.; Conner, W. C. *Langmuir* **1994**, *10*, 1556.
(66) Deboer, J. H.; Linsen, B. G.; Osinga, T. J. *J. Catal.* **1965**, *4*, 643.

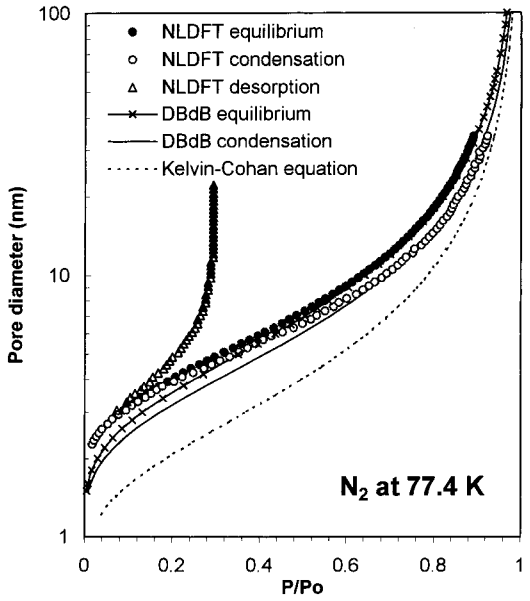

Figure 2. Pore size dependence for the equilibrium and spontaneous capillary condensation/desorption transitions of N_2 at 77 K in spherical pores of siliceous materials. NLDFT spontaneous condensation (open circles); NLDFT equilibrium transitions (closed circles); NLDFT spontaneous desorption (triangles). Capillary condensation (solid line) and equilibrium pressure (solid line, crosses) from Derjaguin−Broekhoff−de Boer theory; Kelvin−Cohan equation for the spherical interface (dotted line).

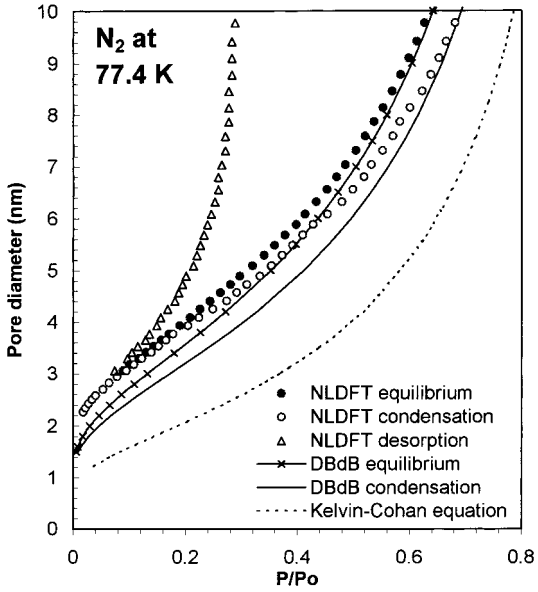

Figure 3. See legend to Figure 2.

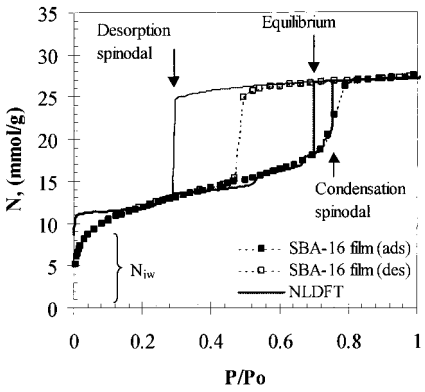

Figure 4. Comparison of the experimental nitrogen adsorption isotherm on SBA-16 material (ref 42) with the NLDFT isotherm in a spherical pore of 12.1 nm in diameter ($34\sigma_{ff}$). The theoretical hysteresis loop is bounded by the vertical lines of spontaneous adsorption (right) and desorption (left). The equilibrium transition (middle line) is not observed experimentally. To account for the intrawall porosity of SBA-16 (see text), the theoretical isotherm is shifted upward by $N_{iw} = 8.66$ mmol/g.

spontaneous transitions are shifted to lower relative pressures; (2) the hysteresis loop bounded by the vaporlike spinodal and equilibrium pressures is narrower than in the cylindrical pore of the same diameter; (3) the capillary critical pore size, which corresponds to the disappearance of the capillary condensation transition, is larger than in the cylindrical geometry. In our case, the capillary critical pore size is ca. $D_{in} = 2.5$ nm ($2R = 8.7\sigma_{ff}$).

An artificial stepwise behavior of the theoretical isotherms in the region of multilayer adsorption is caused by simplifications used in the model, namely, the structureless pore walls and the spherically symmetric density distribution. Nevertheless, as we have shown earlier for the case of cylindrical pores, these simplifications do not affect the ability of the theory to predict the capillary condensation transitions in nanopores.[28,32,59]

In Figures 2 and 3, we present the relative pressures of the spontaneous capillary condensation, spontaneous desorption, and equilibrium transitions in spherical pores of different diameters. The pressure−pore size dependencies merge at the capillary critical point $D_{in} = 2.5$ nm ($D = 8.7\sigma_{ff}$). As the pore size increases, the pressures of spontaneous desorption asymptotically approach the relative pressure of ca. $P/P_0 = 0.3$, which corresponds to the spinodal point of bulk nitrogen in the DFT model.[61] In pores larger than ca. 10 nm, the NLDFT line of spontaneous capillary condensation asymptotically approaches the result of the DBdB theory.[50] Similarly, the NLDFT line of equilibrium transitions in pores of >10 nm asymptotically approaches the DBdB result. In smaller pores, there are substantial deviations between the NLDFT and DBdB predictions, especially for the pressure of spontaneous capillary condensation. The Kelvin−Cohan equation for the spherical interface substantially overestimates the pressures of capillary condensation. In nanopores of size <10 nm in diameter, the use of the Kelvin−Cohan equation for pore size distribution calculations (BJH method) would lead to the difference of up to 100% (!) as compared to the NLDFT model (Figure 3).

3.3. Comparison with Experiments. Previously, we have shown that in materials with cylindrical pores wider than ca. 5 nm in diameter, capillary condensation occurs very close to the pressure of spontaneous capillary condensation predicted by the NLDFT model.[32,59,61] Thus, in sufficiently wide spheroidal cavities we can expect similar behavior. This expectation is indeed observed as follows from the comparison of the theoretical isotherm in a spherical pore of 12.1 nm in diameter with experimental data on a sample of SBA-16 material[42] (Figure 4). The predicted pressure of spontaneous capillary condensation corresponds to the adsorption step on the experimental isotherm. To fit the density at the total loading, it was necessary to shift the theoretical isotherm upward to account for adsorption in *intrawall* pores. The intrawall pores, which include micropores and narrow mesopores, have been shown to contribute significantly to the total porosity in SBA-15 materials.[36] The intrawall porosity in the materials templated by PEO−PPO−PEO type triblock copolymers arises from interpenetration of PEO segments

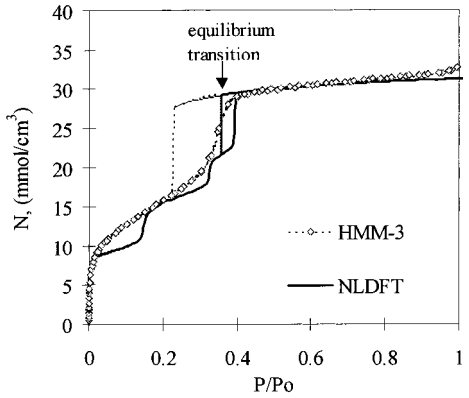

Figure 5. Comparison of the experimental nitrogen adsorption isotherm on HMM-3 material (ref 12) with the NLDFT isotherm in a spherical pore of 5.44 nm in diameter ($16\sigma_{ff}$). The theoretical hysteresis loop is bounded by the vertical lines of spontaneous adsorption (right), equilibrium (middle), and spontaneous desorption (left) transitions.

and the silica matrix.[67,68] The experimental desorption branch on this SBA-16 sample terminates at the relative pressure of ca. 0.48. The experimental desorption step lies between the theoretical pressures of spontaneous desorption and equilibrium transition. As was noted above, the experimental desorption branch is likely to be unsuitable for pore size analysis due to its proximity to the lower closure point of the nitrogen hysteresis loop. From the comparison presented in Figure 4, we conclude that the NLDFT predictions for the capillary condensation are in good agreement with the experimental adsorption data for materials with sufficiently large pores. Additional arguments supporting this interpretation of the results presented in Figure 4 will be given below. It will be demonstrated that the pore diameters of SBA-16 materials determined by the NLDFT method are in remarkably good agreement with the estimates obtained from geometrical considerations.

Figure 5 illustrates the phenomenon of reversible capillary condensation in spherical cavities. We show the experimental isotherm on HMM-3 hybrid organic–inorganic material.[12] Its structure belongs to the *Pm*3*n* space group. The reversible step on the experimental isotherm indicates reversible capillary condensation. The experimental isotherm is in good agreement with the equilibrium NLDFT isotherm in 5.44 nm spherical pores.

4. NLDFT Method for Calculating Pore Size Distributions in Materials with Cagelike Pores

4.1 The Method. For a single spherical cavity, NLDFT predicts discontinuous, vertical capillary condensation steps. In experimental measurements, however, the capillary condensation steps are not discontinuous but rather smooth and rounded. The primary cause for the finite slope of the capillary condensation step is the pore size distribution in the material. Finite size effects in narrow pores also contribute to the rounding of the experimental capillary condensation steps. In what follows, we neglect the influence of the finite size effects and attribute the slope of the experimental capillary condensation steps entirely to the pore size distribution effect.

To calculate the pore size distribution of cavities, the experimental isotherm is represented as a combination of

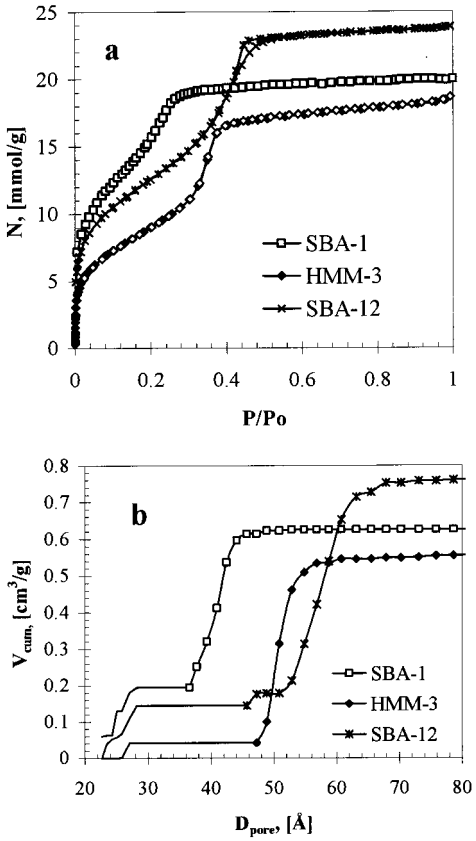

Figure 6. (a) Adsorption isotherms and (b) NLDFT cumulative pore volume distributions of cubic mesoporous materials SBA-1 (ref 70) and HMM-3 (ref 12) (*Pm*3*n* symmetry group) and 3D hexagonal mesoporous material SBA-12 (ref 9) ($P6_3/mmc$ symmetry group). Pore size distributions were calculated using equilibrium NLDFT isotherms in spherical cavities.

theoretical isotherms in individual pores:

$$N_{exp}(P/P_0) = \int_{D_{min}}^{D_{max}} N_V^{ex}(D_{in},P/P_0)\varphi_V(D_{in})\,dD_{in} \quad (8)$$

Here, $N_V^{ex}(D_{in},P/P_0)$ is a kernel of the theoretical isotherms in pores of different diameters; $\varphi_V(D_{in})$ is the PSD function.

Two kernels of theoretical isotherms were calculated. The first kernel consists of the equilibrium isotherms. It is used for PSD calculations from reversible experimental isotherms. The second kernel consists of the metastable adsorption branches. It is used for PSD calculations from the adsorption branches of hysteretic experimental isotherms. To find a PSD function, the integral eq 8 is represented as a matrix equation with pores spanning logarithmically the range from 2 to 50 nm. Solution is found using the nonnegative least squares procedure.[69]

4.2. Pore Size Distribution Characterization of Templated Nanoporous Silicas. *Reversible Isotherms.* Figure 6a shows typical adsorption isotherms on high-quality SBA-1,[70] HMM-3,[12] and SBA-12[9] materials presented in the literature. The isotherms are reversible. Minor hysteresis on the isotherm for the SBA-12 sample was neglected. We calculated PSDs using the equilibrium NLDFT isotherms for spherical cavities. Cumulative PSD plots exhibit prominent steps related to the filling of the regular cavities (Figure 6b). The mean cavity diameter

(67) De Paul, S. M.; Zwanziger, J. W.; Ulrich, R.; Wiesner, U.; Spiess, H. W. *J. Am. Chem. Soc.* **1999**, *121*, 5727.
(68) Kruk, M.; Jaroniec, M.; Ko, C. H.; Ryoo, R. *Chem. Mater.* **2000**, *12*, 1961.
(69) Lawson, C. L.; Hanson, R. J. *Solving Least Squares Problems*; SIAM: Philadelphia, 1995.
(70) Kruk, M.; Jaroniec, M.; Ryoo, R.; Kim, J. M. *Chem. Mater.* **1999**, *11*, 2568.

Table 2. Pore Structure Parameters of Cubic and 3D Hexagonal Regular Nanoporous Materials Determined from Adsorption Isotherms Using Different Methods

material	ref	symmetry	surfactant	unit cell[a] (nm)	reported pore diam (nm)	NLDFT method data[d]					spherical model		cellular model	
						D_{NLDFT} (nm)	V_{tot} (cm^3/g)	V_{iw} (cm^3/g)	S_{me} (m^2/g)	S_{me}/V_{me} (nm^{-1})	D_{me} (nm)	h_{min} (nm)	S_{me}/V_{me} (nm^{-1})	$\langle h \rangle$ (nm)
HMM-3	12	*Pm*3*n*	C_{16}TMACl	11.1	2.9[a]	5.1	0.57	0.04	600	1.12	5.2[e]	1.1[g]	1.26[h]	2.1[i]
SBA-1	70	*Pm*3*n*	C_{16}TEABr	7.87	3.0[b]	4.1	0.63	0.2	620	1.44	3.6[e]	0.3[g]	1.83[h]	1.7[i]
organosilica	41	*Pm*3*n*	C_{16}TMACl	11.0	4.0[b]	5.9	0.64	0.07	590	1.04	5.5[e]	0.3[g]	1.20[h]	1.6[i]
SBA-16	9	*Im*3*m*	$EO_{106}PO_{70}EO_{106}$	16.6	5.4[a]	8.5	0.41	0.28	93	0.71	8.7[e]	5.9[g]	0.75[h]	15[i]
SBA-16 film	42	*Im*3*m*	$EO_{106}PO_{70}EO_{106}$	16.0	9.0[a]	12.2	0.89	0.31	270	0.47	11.9[e]	1.8[g]	0.55[h]	4.8[i]
SBA-12-1	9	$P6_3/mmc$	$C_{18}EO_{10}$	6.34	3.1[a]	5.8	0.76	0.15	595	0.97	5.6[f]	0.5[g]	n/a	n/a
SBA-12	11	$P6_3/mmc$	$C_{18}EO_{10}$	7.43	5.4[c]	6.1	0.45	0.05	380	0.95	6.3[f]	1.3[g]	n/a	n/a
silica fiber	83	$P6_3/mmc$	$EO_{106}PO_{70}EO_{106}$	13.2	6.3[a]	9.4	0.33	0.15	115	0.62	9.0[f]	3.8[g]	n/a	n/a
SBA-2	84	$P6_3/mmc$	C_{16-3-1}	4.90	2.5[a]	4.4[j]	0.53[j]	0			4.4[f]	0.5[g]	n/a	n/a
HMM-2	85	$P6_3/mmc$	C_{18}TMACl	5.51	3.5[b]	4.7	0.74	0.19	760	1.38	4.7[f]	0.8[g]	n/a	n/a

[a] BJH. [b] Corrected BJH. [c] Broekhoff−de Boer. [d] D_{NLDFT} is the cavity diameter; V_{tot} is the volume of regular cavities and intrawall pores; V_{iw} is the volume of intrawall pores; S_{me} is the surface area of regular cavities. [e] Diameter of regular cavities (eq 10). [f] Diameter of regular cavities (eq 11). [g] Minimal wall thickness (see Table 3 for formulas). [h] Calculated by eq 14. [i] Average wall thickness (eq 16). [j] Estimated.

was determined from the inflection point of the cumulative PSD plot. The total volume of pores was determined from the upper plateau on the cumulative distribution plot. The lower plateau on the cumulative distribution, below the filling of the cavities, was interpreted as the volume of intrawall pores. For clarity, these portions of the PSD plots are shown by solid lines only, while the portions related to regular cages are shown by solid lines and symbols. In the PSD calculations, the pore size was limited by 2 nm. Thus, the method allows us to obtain the volume of intrawall pores without a detailed distribution. Results of PSD analyses are summarized in Table 2.

Hysteretic Isotherms. Figure 7a shows two hysteretic adsorption−desorption isotherms on SBA-16 materials,[9,42] which have larger pores. In this case, the adsorption branches of the isotherms reflect the pore filling of the regular cavities in these materials. As discussed above, the desorption branches are not suitable for PSD analyses because of their proximity to the point of instability of liquid N_2 at P/P_0 of ca. 0.42−0.48. Therefore, we calculated PSDs from the adsorption branches using the NLDFT metastable adsorption isotherms. The pore size distributions (Figure 7b) reveal that SBA-16 materials contain large amounts of intrawall pores, which connect the regular cavities. This is typical for templated inorganic materials synthesized using Pluronic PEO−PPO−PEO type triblock copolymer surfactants. SBA-15 materials, which are the cylindrical counterparts of SBA-16, are known to contain significant amounts of intrawall pores.[36]

5. Geometrical Models of Regular Cubic and 3D Hexagonal Structures: Comparison with Adsorption Method

To describe the structure of nanomaterials templated by cubic and 3D hexagonal mesophases, one can consider three types of geometrical models: (1) regular packing of spherical cages; (2) cellular models of space-filling polyhedra; (3) models of triply periodic minimal surfaces (TPMSs). For highly regular materials, these models can be used to obtain independent estimates of pore diameters, which can be compared with results of the NLDFT method.

Regular packing of spherical micelles[18,71] and models of space-filling polyhedra[71] are standard representations of micellar mesophases in amphiphilic systems (see Figure 8a,c). Body-centered cubic (bcc) and 3D hexagonal (hcp) packing of spherical pores seem to be appropriate models for materials of *Im*3*m* (SBA-16) and $P6_3/mmc$ (SBA-2, SBA-12) symmetry, respectively. On the other hand, *Im*3*m* structures can also be described using a cellular model consisting of Kelvin tetrakaidecahedra (Figure 8d).

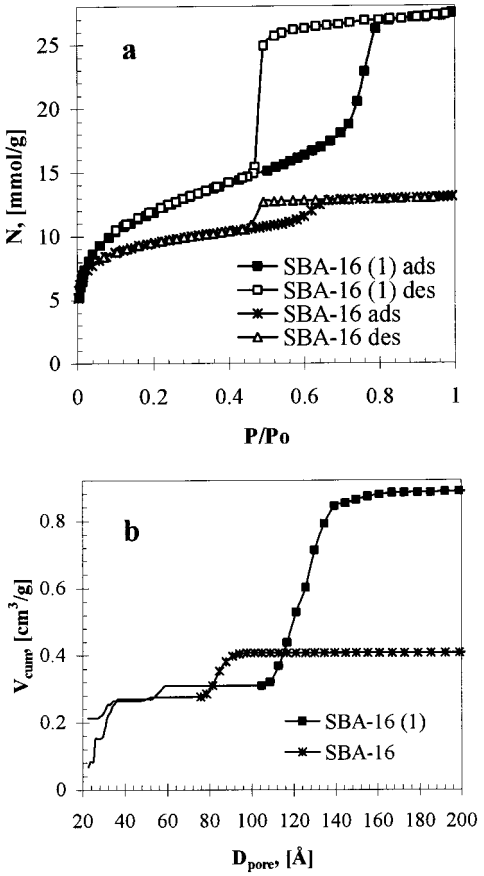

Figure 7. (a) Adsorption isotherms and (b) NLDFT cumulative pore volume distributions of cubic mesoporous materials SBA-16 (refs 9 and 42) (*Im*3*m* symmetry group). Pore size distributions were calculated from the adsorption branches using NLDFT metastable adsorption isotherms in spherical cavities.

There is no simple model of sphere packing for the *Pm*3*n* structure (Figure 8a) because it consists of two types of "micelles" (cavities).[71] The approximation that we used is a cubic lattice with eight cavities per unit cell. The cellular model of *Pm*3*n* structure can be described as tetrakaidecahedra stacked on their hexagonal faces in three sets of perpendicular, mutually interlocking columns, with interstices filled by the dodecahedra[72] (Figure 8b). This structure, derived from the structure of cubic clathrates,[73] has been proposed as a model for dry foams. It gives the best-known partition of space with minimal interfacial

(71) Luzzati, V.; Delacroix, H.; Gulik, A. *J. Phys. II* **1996**, *6*, 405.

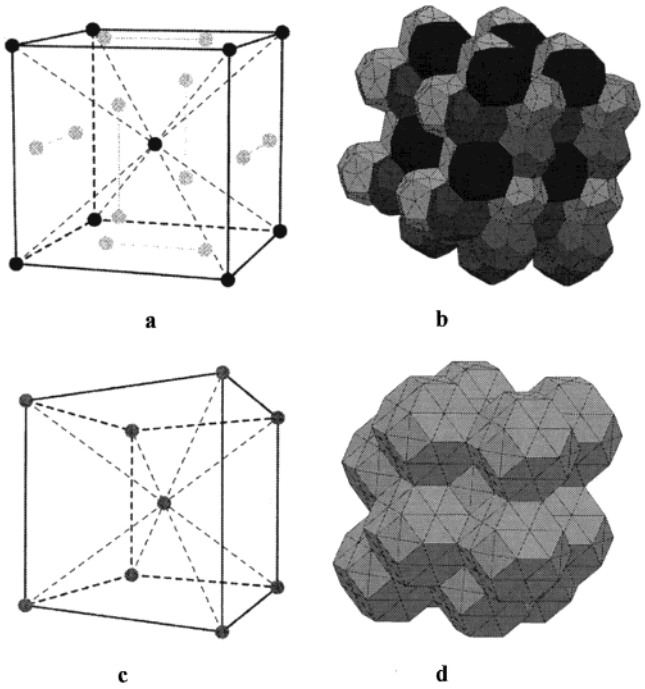

Figure 8. (a) Arrangement of cages in materials with *Pm*3*n* cubic symmetry (adapted from ref 18); (b) polyhedral model of *Pm*3*n* structure; (c) bcc arrangement of cages in materials with *Im*3*m* cubic symmetry (adapted from ref 18); (d) polyhedral model *Im*3*m* structure.

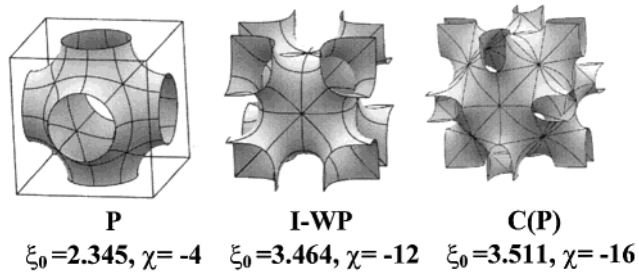

Figure 9. Triply periodic minimal surfaces of *Im*3*m* symmetry. Surface areas and Euler−Poincaré parameters are taken from ref 82; pictures are from ref 86.

area.[72] It has been used to describe micellar phases in lipid-containing systems,[71] oil droplets in lyotropic mixtures,[19] and supramolecular dendrimers.[74] Cellular structures were obtained in Monte Carlo simulations of block copolymers.[75]

In TNM with bicontinuous structure, such as MCM-48, the pore wall is represented as a "swollen" TPMS.[4,30,33−35] Among the materials discussed in this work, only SBA-16 can potentially be modeled as a TPMS. There are several known TPMSs of *Im*3*m* symmetry. For example, Schwartz P and Shoen's I-WP[76] and C(P) (Neovius) surfaces are consistent with the *Im*3*m* space group (Figure 9). Discrimination between different TPMSs can be done based on adsorption data.[30]

Recently, regular mesoporous materials of *Pm*3*n* and *Im*3*m* symmetry have been directly imaged using high-resolution electron microscopy (HREM).[77] An important advantage of the HREM is that no preassumed model is required. The images obtained for the SBA-1 materials of *Pm*3*n* symmetry were consistent with the structure depicted in Figure 8b. The structure of SBA-16 material (*Im*3*m*) was shown to consist of ∼10 nm spherical cavities arranged in a body-centered cubic array and connected through ca. 2 nm openings.[77] The mean cavity surface of SBA-16 was found to be similar to the I-WP minimal surface; however, no quantitative analysis was presented to conclude whether silica walls in SBA-16 actually adopt such a surface.

To determine the internal diameter of the cavities, the HREM method requires the knowledge of the pore volume and the wall density to set a threshold in the potential density and, thus, to differentiate between the amorphous walls and the enclosed cavities.[77] This approach is to a certain extent similar to the use of ideal geometrical models, which is restricted to high-quality materials only, because the pore volumes may be inaccurate due to the presence of uncontrolled impurities or a mixture of different mesophases in the sample. In the gas adsorption method, the capillary condensation pressure gives a reliable and independent measure of the pore diameter.

5.1. The Model of Spherical Cavities. In this model, the spherical cavities are arranged in a regular array. They are connected to each other via windows or openings, which are much narrower than the size of the main cavity. We refer to the volume fraction of regular cavities as *mesoporosity* ϵ_{me}:

$$\epsilon_{me} = \frac{\rho_V V_{me}}{1 + \rho_V V_{tot}} \tag{9}$$

Here, ρ_V is the true density of solid walls (it is assumed to be ∼2.2 g/cm^3 in the case of siliceous materials), V_{me} is the specific volume of the regular cavities, and V_{tot} is the total pore volume. The volume of intrawall pores is thus $V_{iw} = V_{tot} - V_{me}$. Proper separation of the volumes of regular and intrawall pores is very important for materials with substantial amounts of microporosity in the pore walls, for example, SBA-16 and other materials prepared using block-copolymer surfactants.

For a cubic unit cell of length a consisting of ν cavities of diameter D_{me},

$$D_{me} = a\left(\frac{6}{\pi}\frac{\epsilon_{me}}{\nu}\right)^{1/3} \tag{10}$$

For a 3D hexagonal unit cell with the parameters a and c,[17]

$$D_{me} = a\left(\frac{3\sqrt{3}(c/a)}{\pi}\frac{\epsilon_{me}}{\nu}\right)^{1/3} \tag{11}$$

where $(c/a) = 1.633$ for the hexagonal close-packed (hcp) structure. The structural properties of bcc, face-centered cubic (fcc), and hcp packings of spheres are listed in Table 3. The table includes the values for the minimal wall thickness h_{min}, defined as the minimal distance between adjacent cavities. One can introduce also the average wall thickness, h, which for cubic structures can be calculated from the mesoporosity:

(72) Weaire, D.; Phelan, R. *Philos. Mag. Lett.* **1994**, *69*, 107.
(73) Kasper, J. S.; Hagenmul, P.; Pouchard, M.; Cros, C. *Science* **1965**, *150*, 1713.
(74) Hudson, S. D.; Jung, H. T.; Percec, V.; Cho, W. D.; Johansson, G.; Ungar, G.; Balagurusamy, V. S. K. *Science* **1997**, *278*, 449.
(75) Dotera, T. *Phys. Rev. Lett.* **1999**, *82*, 105.
(76) Schoen, A. H. *Infinite periodic minimal surfaces without intersections.* NASA Technical Note TD-5541, 1970.
(77) Sakamoto, Y. H.; Kaneda, M.; Terasaki, O.; Zhao, D. Y.; Kim, J. M.; Stucky, G.; Shim, H. J.; Ryoo, R. *Nature* **2000**, *408*, 449.

Table 3. Parameters of the Geometrical Models of Cubic and 3D Hexagonal Nanomaterials

property	structure			
	cubic	bcc	fcc	hcp
symmetry group	$Pm3n$ (223)	$Im3m$ (229)	$Fm3m$ (225)	$P6_3/mmc$ (194)
number of cavities per unit cell ν	8	2	4	2
minimal wall thickness, h_{min}	$a\frac{\sqrt{5}}{4} - D_{me}$	$a\frac{\sqrt{3}}{2} - D_{me}$	$a\frac{\sqrt{2}}{2} - D_{me}$	$a - D_{me}$
maximum mesoporosity (close packing limit), ϵ_{max}	$\frac{5\pi\sqrt{5}}{48} = 0.7318$	$\frac{\pi\sqrt{3}}{8} = 0.6802$	$\frac{\pi}{3\sqrt{2}} = 0.7405$	$\frac{\pi}{3\sqrt{2}} = 0.7405$
maximum pore volume in the spherical model, $(cm^3/g)^a$	1.240	0.967	1.297	1.297
isoperimetric quotient in the polyhedra model, ζ^b	0.764[c]	0.757	0.7405	

[a] Assuming 2.2 g/cm^3 for the silica wall density. [b] From ref 72. [c] Average value calculated using the Surface Evolver program (refs 79 and 80).

$$h = \frac{D_{me}}{3}\frac{(1-\epsilon_{me})}{\epsilon_{me}} \tag{12}$$

It follows that for a 50% mesoporosity, the average wall thickness is equal to two-thirds of the pore radius. We can also eliminate ϵ_{me} by substituting $\epsilon_{me} = (\pi/6)D_{me}{}^3\nu/a^3$:

$$h = \frac{2a^3}{\pi D_{me}{}^2\nu} - \frac{D_{me}}{3} \tag{13}$$

Equation 13 has an advantage of being independent of absolute quantities (per unit weight). Besides the difficulties with proper determination of the mesoporosity, which requires separation of micro- and mesopores, the absolute quantities may be inaccurate due to the presence of uncontrolled impurities in the sample. In contrast, eq 13 requires only the knowledge of the characteristic pore size, which can be estimated from the capillary condensation pressure.

5.2. Space-Filling Polyhedra Model. In this model, the surface-to-volume ratio is given by the following formula:[71]

$$\frac{S_{me}}{V_{me}} = \left(\frac{1}{a}\right)\left(\frac{36\pi\nu}{\zeta\epsilon_{me}}\right)^{1/3} \tag{14}$$

where ζ is the isoperimetric quotient[72] defined as

$$\zeta = 36\pi V^2/S^3 \tag{15}$$

The values of ζ calculated for different cellular structures are listed in Table 3. Since $Pm3n$ structure consists of two types of polyhedra, ζ given in Table 3 is an average value, which was calculated numerically in ref 78 using the Surface Evolver program.[79,80] Note that for spheres $\zeta = 1$, $D_{me} = 6V_{me}/S_{me}$, and eq 14 transforms into eq 10.

The average wall thickness for the space-filling polyhedra approximation is given by

$$h = 2a\frac{(1-\epsilon_{me})}{\epsilon_{me}}\left(\frac{\zeta\epsilon_{me}}{36\pi\nu}\right)^{1/3} \tag{16}$$

For the spherical model, eq 16 reduces to eq 12.

5.3. Model of Triply Periodic Minimal Surfaces. TPMSs are surfaces of zero mean curvature, $H = (c_1 + c_2)/2 = 0$, and negative Gaussian curvature, $K = c_1c_2 < 0$; here, c_1 and c_2 are the local principal radii of curvature. TPMSs are described by two parameters: the dimensionless surface area $\xi_0 = A_0/a^2$ and the Euler−Poincaré parameter, χ. According to the Gauss−Bonnett theorem, $\chi = \langle K\rangle A_0/2\pi$ (see e.g. refs 81 and 82 for details). In the parallel surface approximation, the area of the parallel surface located at distance l from the midsurface is given by[81]

$$\xi(l) = \xi_0 + 2\pi\chi(l/a)^2 \tag{17}$$

The fraction of voids per unit cell (porosity) is given by

$$\epsilon(l) = 1 - 2\xi_0(l/a) - (4/3)\pi\chi(l/a)^3 \tag{18}$$

Relations between the parameters of TPMSs and the data obtained from adsorption isotherm measurements were given in our previous work.[30] The fraction of regular mesopores obtained from adsorption measurements (eq 9) can be directly compared with the porosity of the model structure calculated from eq 18. The specific surface area of mesopores, S_{meso} (m^2/g), is related to the dimensionless surface area ξ as[30]

$$\xi = (1-\epsilon)\rho_V a(S_{meso}/2) \tag{19}$$

5.4. Comparison of the Results of Adsorption and Geometrical Methods for Pore Size Analysis of Cubic and 3D Hexagonal Templated Nanoporous Silicas. The mesoporosity was calculated from eq 9 using the total pore volume and the volume of intrawall pores determined from the NLDFT pore size distributions. The "geometrical" pore diameters were calculated from eqs 10 and 11 (for cubic and 3D hexagonal structures, respectively). Comparison of the NLDFT pore diameters with those obtained from geometrical considerations is presented in Figure 10 and in Table 2. The agreement is truly remarkable. In Figure 11, we plotted the reduced pore radii versus the fraction of spherical cavities for the bcc, hcp, and simple cubic packings. The points represent data obtained by the NLDFT method from adsorption isotherms on SBA-16, SBA-12, and SBA-1 materials, respectively. The experimental data points are in very good agreement with the expected models of the pore structure. Thus, the NLDFT method helps to discriminate the morphological symmetry of regular nanomaterials.

(78) Weaire, D.; Phelan, R. *Philos. Trans. R. Soc. London, Ser. A* **1996**, *354*, 1989.
(79) Brakke, K. *Experimental Mathematics* **1992**, *1*, 141.
(80) Brakke, K. http://www.susqu.edu/facstaff/b/brakke/evolver/.
(81) Hyde, S. T.; Ninham, B. W.; Zemb, T. *J. Phys. Chem.* **1989**, *93*, 1464.
(82) Schwarz, U. S.; Gompper, G. *J. Chem. Phys.* **2000**, *112*, 3792.
(83) Yang, P. D.; Zhao, D. Y.; Chmelka, B. F.; Stucky, G. D. *Chem. Mater.* **1998**, *10*, 2033.
(84) Hunter, H. M. A.; Wright, P. A. *Microporous Mesoporous Mater.* **2001**, *43*, 361.
(85) Kruk, M.; Jaroniec, M.; Guan, S. Y.; Inagaki, S. *J. Phys. Chem. B* **2001**, *105*, 681.
(86) Brakke, K. http://www.susqu.edu/facstaff/b/brakke/evolver/examples/periodic/periodic.html.

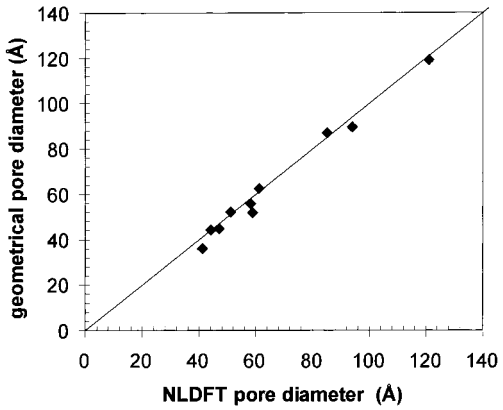

Figure 10. Comparison of the pore diameters determined by the NLDFT method and the geometrical models of sphere packing (data from Table 2).

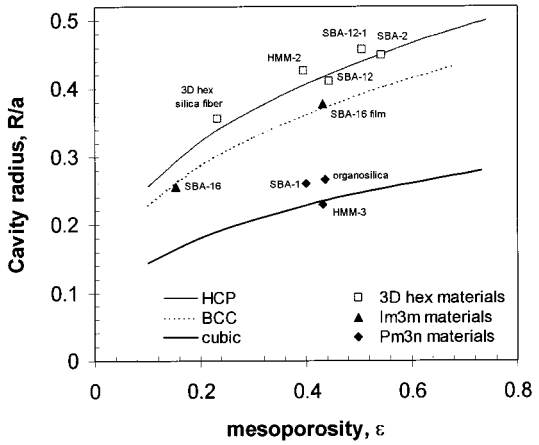

Figure 11. Reduced pore radii of regular materials with cagelike pores as a function of the volume fraction of cavities. Experimental pore structure parameters obtained by the NLDFT method are compared with the corresponding models of ideal packing of spheres.

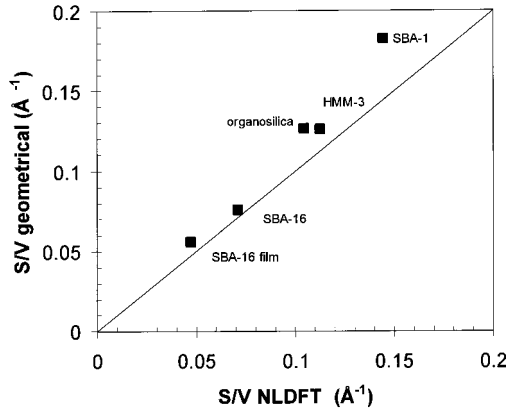

Figure 12. Surface-to-volume ratios for materials with cubic structure determined by the NLDFT method and cellular models of space-filling polyhedra (data from Table 2).

For *Pm*3*n* and *Im*3*m* materials, we have also applied the cellular models of space-filling polyhedra. The surface-to-volume ratios calculated from eq 14 were compared with the NLDFT data (Table 2, Figure 12). Agreement between the geometrical and NLDFT-calculated S_{meso}/V_{meso} ratios is good except for the smallest pore SBA-1 sample[70] (Figure 12). We conclude that for the cagelike materials with significant amount of intrawall pores, for example, cubic SBA-16[9,42] templated by triblock copolymers, the NLDFT method allows one to separate the contributions from the regular cavities and intrawall pores quite accurately.

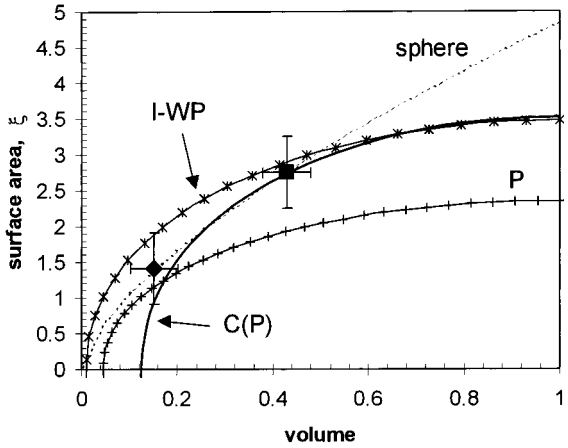

Figure 13. Surface area versus pore volume for different models of *Im*3*m* structures (lines). Data for SBA-16 materials (refs 9 and 42) were obtained from nitrogen adsorption isotherms using the NLDFT method for spherical pores (points).

Finally, we compared the NLDFT pore structure parameters of SBA-16 materials with the TPMS geometrical models of *Im*3*m* symmetry. In Figure 13, we plot the surface area versus pore volume for different *Im*3*m* parallel surfaces in comparison with the NLDFT data obtained for SBA-16 materials. The error bars (0.05 in volume and 0.5 in surface units) reflect approximately the error involved in the separation of the volumes of the main cavities and intrawall pores. For comparison, we also plot the surface−volume relation for the spherical model. As can be seen, I-WP and C(P) structures appear to be more consistent with the adsorption data than the P surface. However, having only two experimental points, we cannot discriminate between I-WP and C(P) morphologies. Determination of the diameter of pore openings may provide further useful information.

Although the simple model of spherical cavities is in remarkably good agreement with adsorption data on SBA-16, it is also not very surprising that the experimental data are quite consistent with other structural models too, such as the Kelvin polyhedra model and the I-WP and C(P) minimal surface models. The capillary condensation pressure is determined by the curvature of the liquid−gas interface and the strength of the solid−fluid attraction in the confinement. These properties are quite similar in the geometrical models of the *Im*3*m* cagelike structures considered (Figures 8d and 9). This fact has important positive implications for the characterization of materials with cagelike structures. It demonstrates that the spherical pore model is a reasonable approximation for a broad range of materials with cagelike pores.

6. Conclusions

We have studied nitrogen adsorption and capillary condensation in spherical nanopores with silica walls using the NLDFT. The results show that in sufficiently small cavities (pore diameters $3 < D < 6$ nm) capillary condensation occurs reversibly, and the equilibrium condensation pressure is determined by the diameter of the cavity. In larger cavities (>6 nm), the equilibrium transition is not observed. Instead, the capillary condensation occurs irreversibly at the relative pressure which is very close to the predicted spinodal point of the metastable adsorption branch. Desorption from larger

cavities is determined by the size of the windows, which connect the cavity with the bulk fluid. If the size of the window is smaller than a certain critical size (ca. 4 nm for N_2 at 77 K) or, equivalently, the equilibrium evaporation pressure from the pore window is lower than a certain critical relative pressure, the confined fluid attains its limit of stability, and spontaneous desorption occurs via cavitation. The NLDFT predicts quantitatively the relative pressures of reversible (equilibrium) and spontaneous (spinodal) capillary condensation transitions of N_2 in regular siliceous materials with cagelike, spheroidal nanopores. For pores larger than ca. 10 nm in diameter, the NLDFT predictions merge with the results of macroscopic Derjaguin−Broekhoff−de Boer theory, while in smaller pores the deviations between the molecular and macroscopic approaches become significant. The conventional Kelvin−Cohan equation for a spherical meniscus, the basis of the BJH method of PSD analysis, becomes progressively inaccurate for pores less than ca. 100 nm in diameter. Consequently, the BJH method may underestimate the pore diameters of cagelike materials by almost 100% (Figures 2 and 3).

We have developed a new NLDFT-based method for calculating pore size distributions from adsorption isotherms. The NLDFT method allows one to calculate the PSD of the cages, the total pore volume and surface area, the amount of intrawall porosity, and, in combination with the X-ray diffraction measurements, the pore wall thickness. The method has been applied to characterization of templated nanoporous materials with ordered cubic $Pm3n$ (SBA-1, HMM-3), cubic $Im3m$ (SBA-16), and 3D hexagonal $P6_3/mmc$ (SBA-2, SBA-12) symmetries. Several geometrical models have been used to obtain independent estimates of the pore size in these regular materials: models of sphere packing (for $Pm3n$, $Im3m$, and $P6_3/mmc$ structures), cellular models of space-filling polyhedra (for $Pm3n$ and $Im3m$ structures), and periodic minimal surface models (for $Im3m$ structures). The pore structure parameters obtained by the NLDFT method are in remarkably good agreement with the results obtained from geometrical considerations, especially using the models of regular sphere packing (bcc, hcp, etc.). It has been demonstrated that the adsorption method allows one to differentiate between the materials of different morphological symmetry (see Figure 11).

The NLDFT interpretation of adsorption data allows us to validate the suitable pore structure models for different types of TNM. In particular, the adsorption data support that the pore structures of $Pm3n$ cubic SBA-1 and HMM-3 materials are consistent with the structure shown in Figure 8. The pore structure of 3D hexagonal materials (SBA-2, SBA-12) can be rationalized as the hexagonal packing of spherical pores. The structure of SBA-16 is consistent with a body-centered cubic spherical or polyhedra model; however, a bicontinuous structure centered on one of the periodic minimal surfaces of $Im3m$ symmetry, most likely I-WP or C(P), cannot be ruled out also. We also conclude that the pore walls of materials templated by triblock copolymer surfactants contain significant amounts of intrawall pores.

Acknowledgment. This work was supported by the TRI/Princeton exploratory research program. We thank S. Inagaki for the adsorption data on HMM-3 material.

LA0107594